Accepted Manuscript

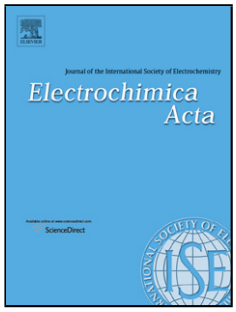

Title: Bean-dreg-derived carbon materials used as superior anode material for lithium-ion batteries

Author: Haohui Ru Kaixiong Xiang Wei Zhou Yirong Zhu Xiu Song Zhao Han Chen

PII: S0013-4686(16)32285-X
DOI: http://dx.doi.org/doi:10.1016/j.electacta.2016.10.202
Reference: EA 28297

To appear in: *Electrochimica Acta*

Received date: 26-8-2016
Revised date: 12-10-2016
Accepted date: 25-10-2016

Please cite this article as: Haohui Ru, Kaixiong Xiang, Wei Zhou, Yirong Zhu, Xiu Song Zhao, Han Chen, Bean-dreg-derived carbon materials used as superior anode material for lithium-ion batteries, Electrochimica Acta http://dx.doi.org/10.1016/j.electacta.2016.10.202

Bean-dreg-derived carbon materials used as superior anode material for lithium-ion batteries

Haohui Ru[a], Kaixiong Xiang[a], Wei Zhou[a], Yirong Zhu[a], Xiu Song Zhao[b], Han Chen [a, *]

[a]College of Metallurgy and Materials Engineering, Hunan University of Technology, Zhuzhou 412007, PR China

[b]School of Chemical Engineering, The University of Queensland, Brisbane, 4072, Australia

Corresponding Author: Han Chen, E-mail: lzdxnchh@126.com, Phone/Fax: +86-731-22183467

Graphical abstract

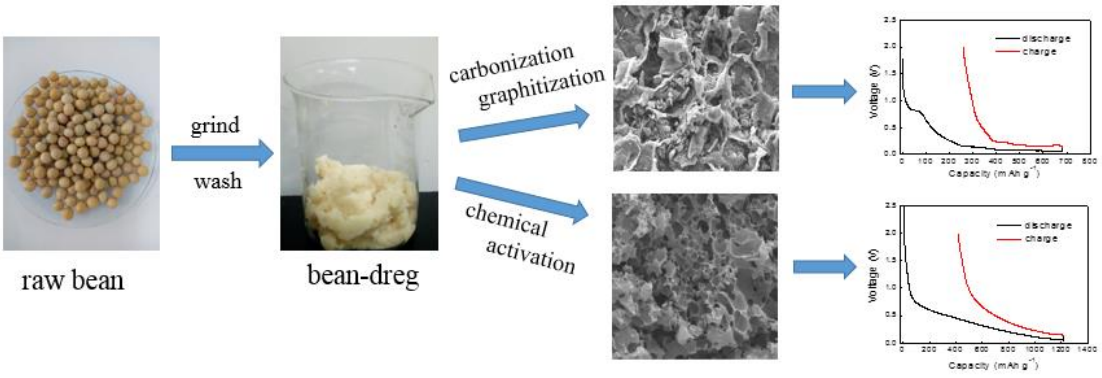

Highlights

1. The structures of modified carbons from bean dregs were regulated via graphitization treatment and chemical activation.

2. The sample thermally treated at 2800 ^{O}C showed more ordered graphitic domains and superior reversibility, excellent cycling stability and rate capability.

3. The KOH-activated sample demonstrated enhanced electrochemical performance due to its high surface area and abundant mesoporous structure.

Abstract

The structures of modified carbons from bean dregs were regulated via graphitization treatment and chemical activation. The microstructure and electrochemical performance were studied using X-ray diffraction, Raman spectrometer, SEM and TEM techniques. The electrochemical performance was investigated using electrochemical methods. After heat-treatment at 2800 ^{O}C, the obtained BDC-2800 possessed a high degree of graphitization and showed an outstanding cycling performance, delivering capacity decay from 423 to 396 mAh g^{-1} at 0.1 C after 100 cycles. The chemical-treated carbons also demonstrated enhanced electrochemical performance, especially for the KOH-treated sample. The BDC-K displayed superior specific charge capacity of 801 mAh g^{-1} at 0.1 C, and showed an impressive rate capability of 643 mAh g^{-1} at 1 C. In addition, this sample delivered capacity retention of 94% after 500 cycles at 1 C. This good electrochemical performance was mainly due to its high surface area and abundant mesoporous structure.

Keywords: Lithium-ion batteries; graphitization; activation; bean dreg

1. Introduction

With the rapid development of economy, the demand for energy is also increasing, especially in hybrid electric vehicles (HEVs) and renewable energy systems. Rechargeable lithium-ion batteries (LIBs) in energy storage field have some advantages of friendly environment, high working voltage, high specific energy, long cycle life etc. [1-7]. As we all known, conventional anode material for LIBs is mainly generated from graphite due to its low cost and electrochemical potential with respect to lithium metal. Unfortunately, theoretical

specific capacity of graphite is only 372 mAh g^{-1}, and its rate performance greatly limits the further improvement for LIBs with high energy and high power [8, 9]. Therefore, many efforts have been made aiming to synthesize new carbonaceous materials for practical applications.

Recently, many attentions have been attracted on next-generation high-capacity anode materials such as Si [10], Sn [11], and their oxides, and transition metal oxides (CuO, MnO_2, Fe_2O_3, Co_3O_4) [12-18]. However, such materials usually exhibit evident volumetric changes during charge/discharge processes, with a large irreversible capacity loss compared to carbonaceous materials [19, 20]. Therefore, more efforts are made to explore suitable carbonaceous materials for high-capacity anodes.

In recent studies, carbonaceous anode materials from biomass source, such as spongy pomelo peels [21], rice husk [22, 23, 24], rice straw [25], sugar cane bagasse [26], coffee beans [27], coconut shells [28], peanut shells [29], have become more and more attractive for their abundance, low cost, easy accessibility and environmental friendliness compared with other carbonaceous precursors. Given this, the application of biomass has received much attention in energy storage field.

As well known, bean dreg is the main byproduct in bean product processes and its yield is very large. Recently some applications on bean dreg have been reported, such as activated carbon [30], supercapacitor [31]，lithium-sulfur battery [32], however its application in anode for lithium-ion battery has hardly been found. Herein, we report a simple and effective strategy in preparing LIB anode material from bean dregs with pyrolysis treatment at different temperatures and further treatment via graphitization and chemical activation. The structure

and electrochemical behavior were subsequently investigated through various characterization techniques.

2. Experimental

2.1 *Preparation of carbons*

The fresh bean dregs (hereafter abbreviated as BD) obtained from the nearby breakfast shop were extensively soaked and washed with distilled water to remove the impurities, and then dried overnight in a vacuum oven. Pyrolysis process was then carried out at 700, 900, 1100 ^{O}C respectively in a nitrogen-flowing tube furnace for 6 h with a heating rate of 5 ^{O}C min^{-1}. The black products were cooled naturally and then thoroughly ground for further use. Three series of bean dreg carbon samples (BDCs) are respectively denoted as BDC-700, BDC-900 and BDC-1100. For further graphitization, BDC-900 sample was further heat-treated at a high temperature of 2800 ^{O}C, denoted as BDC-2800. Particularly, the graphitizing treatment was carried out with a vacuum induction furnace (Electric Furnace Plant of Jinzhou in Liaoning, China) in institute of novel carbon materials, Hunan University.

In a separate experiment, the fresh bean dregs were respectively treated with concentrated solutions of $ZnCl_2$ and KOH porogens at mass ratio of 1:5 (dreg : porogen), and ultrasoniced at 60 ^{O}C then dried at 100 ^{O}C. The above sample was heated at 900 ^{O}C for 2 h. The pore-former was removed with dilute nitric acid and distilled water. The prepared carbons treated with $ZnCl_2$ and KOH were respectively denoted as BDC-Z and BDC-K.

2.2 *Material Characterization*

The carbon weight percentages of the samples were determined on CS-600. The hydrogen, nitrogen and oxygen weight percentages of the samples were determined on an

ONH Analyzer. X-ray diffraction patterns (XRD) were recorded on a Siemens D5000 using the Cu Kα radiation of (λ= 1.5418 Å). The microscopic feature of the samples was characterized by field-emission scanning electron microscopy (FESEM) (JSM-6700F, JEOL, Tokyo, Japan) with the energy dispersive X-ray (EDX) microanalysis. Transmission electron microscopy (TEM) images were obtained with a JEOL 2010 microscope operating at 200 keV. Raman spectra were obtained by using a Renishaw Invia system, under λ=514 nm laser excitation. Nitrogen adsorption and desorption isotherms were determined with a Micrometeretics ASAP 2020 analyzer. Specific surface areas were estimated according to the BET model, and pore size distributions were calculated by using the BJH method.

2.3 *Electrochemical testing*

The working electrode was prepared by mixing the active materials, acetylene black, and polyvinylidene fluoride (PVDF) in a weight ratio of 85:5:10 with N-methylpyrrolidone (NMP) as a solvent. The resulting slurries were cast onto a common Cu foil, dried at 50 ^{O}C for 24 h and rolled into 25 μm thin sheets. The film was cut into disks with a diameter of 14 mm, and then dried in vacuum at 120 ^{O}C for 24 h. CR2025 coin-type cells were assembled in an Ar-filled glove box with lithium foils as the counter electrodes and polypropylene microporous films (Celgard2400) as separators. The liquid electrolyte is 1mol L^{-1} $LiPF_6$ in a mixture of ethylene carbonate (EC) and dimethyl carbonate (DMC) (1:1, v/v). The galvanostatic charge and discharge tests were carried out on LAND testing instrument in a voltage range between 0 and 2 V at 0.1 C, 0.5 C and 1 C (with respect to the theoretical value of 372 mAh g^{-1} for graphite). Cyclic voltammetry (CV) was conducted on a CHI660D electrochemical workstation in the voltage range of 0.0-2.0 V at a scan rate of 0.1 mV s^{-1}.

3. Results and Discussion

The compositions of the pyrolytic carbons were presented in Table 1. The pyrolytic carbons mainly consist of C, H, O, N elements (by weight) and hardly contain other heteroatoms. This is corroborated by the EDX microanalysis of all samples. As expected, with increasing carbonization temperature, there is a significant increase in carbon content and simultaneously decrease in oxygen content. The X-ray patterns of the three samples are displayed in Fig. 1a. The broad peak around 24^{O} is attributed to the (002) crystal plane of parallel-stacked graphene sheets, while the peak around 43^{O} is due to the (100) crystal plane of sp^2 hybridized carbon [33]. The XRD patterns also show that all the samples contain amorphous carbon, which is beneficial to lithium ion intercalation and deintercalation [34]. The average graphite interlayer spacing (d_{002}), the thickness (Lc) and average width (La) of the graphitic domains are usually used to characterize the graphite crystallite changes. As Table 2 shows, with the increase of pyrolysis temperature, it is calculated that d_{002} decreases from 0.3675 to 0.3573 nm, while La and Lc increases. These results demonstrate that high pyrolysis temperature created more ordered stacked graphite layers and larger graphite crystallite. Moreover, carbon pyrolyzed at high temperature shows improved electric conductivity, which is favorable for electrochemical performance.

Fig. 1b shows the fitted Raman spectra for the three BDC samples. The D band at 1349 cm^{-1} corresponds to disordered carbon or defective graphitic structures, while the G band at 1585 cm^{-1} is a characteristic feature of sp^2 graphitic structure [35]. The intensity ratio of the G band to the D band (I_G/I_D) indicates the degree of graphitization in the carbons. The higher the ratio is, the greater the degree of graphitization of the carbon [36, 37]. The ratios of I_G/I_D for

BDC-700, 900, 1100 are respectively 0.79, 0.82 and 1.10 (shown in Table 2). This result suggests that an increase in pyrolysis temperature leads to a higher degree of graphitization, which is consistent with the XRD results.

Fig. 1c shows the nitrogen adsorption–desorption isotherms of samples. According to the IUPAC classification, all samples display a type-IV isotherm, indicating the presence of that a large quantity of mesopores [38]. The existence of hysteresis loop at $P/P_o > 0.4$ is due to capillary condensation within mesoporous [39]. The Barrett-Joyner-Halenda (BJH) pore size distribution curves of the samples shown in Fig. 1d demonstrate the presence of both mesopores (pore diameters between 2~50 nm) and micropores (pore diameters less than 2 nm). These mesopores offer the channels for electrolyte penetration and lithium ion transportation. The detailed pore structure parameters of the BDCs samples are shown in Table 2. It is clearly seen that the surface area increases first and then decreases with the increase in temperature from 700 ^{O}C to 1100 ^{O}C, indicating the pore structure changes with temperature. The BDC-900 sample exhibits the highest surface area and relatively modest porosity. Such unique properties are in favor of Li storage and improving the capacity.

Figs. 1e-g show the SEM images of the BDC samples. It is seen that the morphology of the samples is similar. Sample BDC-1100 has more fragments and takes on a smaller particle size than BDC-700 and BDC-900. This is because that carbon pyrolyzed at a higher temperature contains a larger amount of graphitic domains, which may be more easily crushed during the grinding process [21]. This result also can be supported by the XRD and Raman results.

The electrochemical performances of the BDC samples as anode materials for lithium

ion batteries were studied. Figs. 2a-c show the first three charge/discharge curves of BDC-700, BDC-900 and BDC-1100 electrodes at current rate of 0.1C. In the first cycle, the discharge capacity of the three samples are 823, 886 and 743 mAh g^{-1}, and the charge capacities are 395, 445, and 384 mAh g^{-1}, respectively. The corresponding Coulombic efficiencies of the three samples are 48.0%, 50.2% and 51.7%, respectively. The irreversible capacity can be ascribed to the formation of solid electrolyte interphase (SEI) film during the first cycle and/or the irreversible lithium insertion the carbon matrix [40, 41]. The charge capacities of BDC-700, BDC-900 and BDC-1100 are 372, 433 and 377 mAh g^{-1} in the second cycle, and the Coulombic efficiencies increase dramatically to 91.6%, 95.2% and 96.4%. As the cycling continued to the 3rd cycle, the Coulombic efficiencies of three sampes all maintain over 97%, indicating a stable SEI film has been established and the carbon electrode materials are stabilized. With increasing pyrolysis temperature, more pores are formed to accommodate lithium ions, thus improving the reversible capacity, while on the other hand the growth of graphitic carbon leads to the capacity deterioration because graphitic carbon has lower capacity than amorphous carbon. BDC-900 compromises the porous properties and graphitic carbon, therefore it exhibits the highest charge capacity [42].

Figs. 2d-f show the CV curves for BDC samples at a scan rate of 0.1 mV s^{-1} in the voltage range of 0.0-2.0 V. All curves share the same feature, namely the initial cycle is different from the subsequent cycles. The strong reduction peak at 0.75 V can be seen from the first cycle, but this peak disappeared in the subsequent cycles. This phenomenon is usually due to the decomposition of electrolyte and the formation of SEI film. The reduction peak at 0.25 V is a result of irreversible lithium storage like trap of Li^+ in mesopores [43]. In addition,

the distinct reduction peak at approximately 0 V might originate from the intercalation of lithium ion in graphitic carbon. The sharp oxidation peak between 0 V and 0.5 V corresponds to the deintercalation of lithium ions from graphite carbon [44, 45]. Particularly, the reduction peak areas in the first cycle are obvious larger than the following ones. The extra area can be attributed to the formation of SEI film, which results in the larger discharge capacity of the first cycle than the second cycle. In addition, the CV curves after the first cycle are nearly overlapping with each other, indicating the stabilization of SEI film and carbon structure. These results are well consistent with the discharge/charge results.

As mentioned above, BDC-900 shows the apparent advantage in discharge/charge performance among the samples. Here, cycling performance and Coulombic efficiency of the BDC-900 electrode evaluated at a current density of 0.1C are displayed in Fig. 2g. It can be clearly seen that BDC-900 displays an obvious capacity reduction upon cycling. After 100 cycles, it only keeps a reversible capacity of 344 mAh g^{-1}, 77.3% of its initial capacity, revealing its undesirable reversible insertion/extraction process of Li ions into/from the carbon material. The rate capability of BDC-900 electrode was also evaluated (Fig. 2h). The BDC-900 electrode exhibits charge capacities around 445, 317 and 191 mAh g^{-1} when cycled at a rate of 0.1 C, 0.5 C and 1 C, respectively. After 500 cycles at a high rate of 1 C, the BDC-900 electrode retains a reversible capacity of 100 mAh g^{-1}, keeping 52.4% of its initial capacity. These results highlight that the BDC-900 electrode does not perform well in cycling and rate capability.

Although BDC-900 sample exhibits the best discharge/charge performance among the series BDCs, the low Coulombic efficiency in first cycle, low specific capacity, poor cycling

stability and rate capability are still serious issues that need to be solved. As we know, when pyrolyzed at a temperature above 2000 ^{O}C, carbon materials usually possess large amount of ordered carbon sheets due to the relaxing of the turbostratic disorder and takes on a lithium-insertion characteristic similar to graphite, thus the capacity of carbon materials can be increased [46]. In this case, the BDC-900 sample was heated at 2800 ^{O}C for further graphitization to improve its electrochemical performance.

Fig. 3a shows the XRD patterns of BDC-2800, along with that of graphite. The XRD pattern shape of BDC-2800 is significantly different from BDC-900. When the temperature increased to 2800 ^{O}C, the (002) peak approximately shifts from 24^{O} to 26^{O} and becomes stronger in intensity. Besides, coupled with the inset of Fig. 3a, BDC-2800 exhibits similar peaks to graphite, especially the appearance of (100), (101), (102), but they are distinctly weaker than graphite. Moreover, the d_{002} value of BDC-2800 must be noted, 0.3371 nm (Table 3), which is much smaller than that of BDC-900 (0.3694 nm) and close to the value for graphite (0.3354 nm). Besides, the La and Lc of BDC-2800 greatly increase compared to BDC-900, indicating the growth of crystallites at high temperature of 2800 ^{O}C. Therefore, the BDC-2800 sample consists of large domains of parallel-stacked graphene sheets and reflects its good crystallinity. The graphitization degree of BDC-2800 is characterized in Raman spectra in Fig. 3b. As noted before, the I_G/I_D value is only 0.85 for BDC-900. Whereas the value increases to 2.30 for BDC-2800, indicating the ultrahigh temperature leads to more ordered crystalline. Such a conclusion is highly accordance with XRD results.

The SEM image of BDC-2800 in Fig. 3c shows that the pyrolytic carbon has a smaller particle size because large amount of graphitic structures are distributed within carbon, which

can be more easily destroyed at such a high temperature. Figs. 3d and e display TEM images of BDC-900 and Figs. 3g and h depict ones of BDC-2800. It is apparently confirmed that BDC-2800 exhibits smaller particle size than BDC-900. The HRTEM microphotograph in Fig. 3f clearly reveals that BDC-900 displays fewer ordered graphitic crystallites in certain regions (circled with the red line), and definitely they are referred to graphitic (002) crystal planes. The characteristic lattice fringe of the (002) crystal plane is magnified in the inset of Fig. 3f. As seen from Fig. 3i, BDC-2800 shows more ordered graphitic crystallites are widely embedded within the amorphous carbon material, which further illustrates that graphitic crystallites are coated by amorphous carbons. The lattice fringe and interlayer spacing in the inset of Fig. 3i indicate its good crystallinity. These observations validate the results of XRD and Raman analysis.

Fig. 4a shows the galvanostatic charge-discharge curves of BDC-2800. The discharge and charge capacities in the first cycle are 681 and 423 mAh g^{-1}, corresponding to a Coulombic efficiency of 62.1%, which is also ascribed to the formation of SEI film. Although the capacities of BDC-2800 are much lower than BDC-900 due to the existence of more ordered graphitic carbons in BDC-2800 resulting in capacity deterioration, a higher Coulombic efficiency demonstrates its improved reversibility, which seems to be related to the smaller particles and crystallite size for BDC-2800. The discharge and charge capacities are 423 and 419 mAh g^{-1} in the second cycle and the Coulombic efficiency reaches over 99%. The 3rd cycle is almost overlapping with the second one, revealing the excellent reversibility towards lithium insertion-extraction. It is worthy to note that three voltage plateaus are observed in the first discharge cycle. The discharge voltage plateau at about 0.8 V results from

the formation of SEI film and disappears in the subsequent cycles. The second voltage plateau at around 0.2 V is a characteristic plateau of amorphous carbon, which is commonly displayed in previous discharge/charge curves of BDC-700, 900 and 1100. The flat voltage plateau below 0.2 V, corresponding to characteristic of graphite structure, can be observed in the subsequent cycles, implying a high graphitization degree of BDC-2800 [47]. This result is consistent with the XRD and Raman results.

Cycling performance and Coulombic efficiency of BDC-2800 were also tested under a current rate of 0.1 C (Fig. 4b). In addition to the improved Coulombic efficiency in first cycle, BDC-2800 exhibits more excellent cycling stability in contrast to BDC-900. The reversible capacity and Coulombic efficiency of BDC-2800 electrode are stabilized at 396 mAh g^{-1} and 99.5% after 100 cycles, which is much better than BDC-900. Besides, this value is still higher than the theoretical capacity of graphite (372 mAh g^{-1}). Generally speaking, the disordered structure gives rise to the increase in capacity because there is more space for Li ions insertion into carbon material [48]. Fig. 4c displays the rate capability and cycling stability of BDC-2800 electrode. The charge capacity decreases from 423 to 331 mAh g^{-1} when the current rate is increased from 0.1 C to 1 C, and drops from 331 to 320 under 1 C after 500 cycles, indicating a high capacity retention over 96%. This extremely superior cycling performance and rate capability are due to the co-existence of amorphous carbon with a certain disordering degree and graphitized carbon with a high graphitization degree.

Generally activation treatment with porogens, such as KOH and $ZnCl_2$, is an effective approach to improve the porosity of activated carbon materials [49-51]. Figs. 5a and b display the XRD patterns and fitted Raman spectra of BDC-Z and BDC-K. As can be seen from the

XRD patterns, that activation with porogens for BDC does not change its original amorphous structure. However, the d_{002}, La and Lc values (Table 4) of BDC-Z and BDC-K increase slightly in contrast to BDC-900. This result is mainly attributed to the yielded gaseous decomposition products during activation process, which further loosening the carbon layers to create more disordered structure [52]. Raman spectra are sensitive to characterize the slight structure changes. Here, as Table 3 shows, the I_G/I_D ratios for BDC-Z and BDC-K are respectively 0.56 and 0.45, which are much lower than that of BDC-900 (I_G/I_D = 0.82). This result demonstrates the activated carbons possess a higher degree of disorder, which is highly accordance with the XRD results.

The more detailed structure properties of activated carbons were investigated by nitrogen adsorption-desorption isotherms. As displayed in Fig. 5c, the BDC-Z and BDC-K still show a type-IV behavior, indicating the mesoporous structures are primary distributed in spite of suffering the activation process. However, the BDC-K and BDC-Z samples deliver a much higher N_2 sorption capacity than BDC-900, demonstrating that more defects or cavities exist in carbons after activation. The corresponding pore size distribution in Fig. 5d further proves its structure characteristic. The mesopores with diameter centered at around 20 nm, which are essentially unchanged compared to the BDC-900. What' more, as Table 3 shows, the BET surface areas of BDC-Z and BDC-K are respectively as high as 827 and 1139 $m^2\ g^{-1}$, which are larger than BDC-900 mainly because of higher porosity, larger pore volume. The average pore diameter of activated carbons is also increased greatly after treated by KOH and $ZnCl_2$.

The morphologies of the resultant chemical-activated carbons are definitely different from the untreated carbons. Figs. 5e and f exhibit the SEM micrographs of BDC-Z and

BDC-K. The BDC-Z sample (Fig. 5e) is primarily made up of nanometer irregular carbon particles without opening pores. Usually, $ZnCl_2$, at high temperature, will not only corrode carbon materials, but also deeply penetrate into inner carbon for more sufficient activation [53]. While the BDC-K sample (Fig. 5f) possesses large quantities pores with diameters from 50 to 200 nm. The generation of these pores results from the activation process by means of KOH corrosion to carbon material and the release of gas at high temperature [54]. The unique structures of BDC-Z and BDC-K could make it plain for the increased specific surface area compared to the untreated carbons. It is believed that either the nanoparticles in BDC-Z or the rich porosity in BDC-K will provide short pathways and high electrical conductivity for rapid diffusion and conduction for both Li ions and electrons.

Figs. 6a and b show the charge/discharge curves of BDC-Z and BDC-K. The first-cycle discharge capacities for BDC-Z and BDC-K are 1038 and 1215 mAh g^{-1}, and the charge capacities are 664 and 801 mAh g^{-1}, corresponding to Coulombic efficiencies of 64.0% and 65.9%. Obviously, the charge capacities are larger than that of BDC-900 and BDC-2800. Although the large capacity loss remains due to the formation of SEI film and the irreversible lithium storage in disordered carbon, it should be noted that the Coulombic efficiencies increase compared to the untreated carbons. This suggests the single layer in carbon may be realigned during the activation process, which sheds additional light on availability of the deep inserted lithium to be “exposed” for the electrochemical cycling [51]. In addition, the more developed porosity after activation provides more pathways to ensure easy accessibility of electrolytes and faster transportation of lithium ions, thus endowing activated carbons with enhanced capacities. The reversible capacities of BDC-Z and BDC-K are 653 and 792 mAh

g^{-1} in the second cycle, and the Coulombic efficiencies increase dramatically to 97.2% and 96.0%. The BDC-Z and BDC-K electrodes exhibit a low trend in capacity fading afterwards.

The cycling performance and Coulombic efficiencies of BDC-Z and BDC-K electrodes conducted at a rate of 0.1 C during the charge/discharge process are shown in Fig. 6c. The BDC-Z and BDC-K electrodes deliver initial charge capacities of 664 and 801 mAh g^{-1} and maintain capacities of 605 and 748 mAh g^{-1} after 100 cycles, indicating only 91.1% and 93.4% capacity retention, whereas the Coulombic efficiencies of them steadily keep nearly 100% after the first cycle. This result is superior to that of BDC-900, demonstrating the BDC material treated with $ZnCl_2$ and KOH has much better cycling performance and higher reversibility than the untreated one. Fig. 6d depicts the rate capability of BDC-900, BDC-Z and BDC-K electrodes tested at different rates. It is clearly seen that the BDC-Z and BDC-K electrodes display more favorable rate performance than BDC-900, especially BDC-K electrode exhibits higher rate capacity at any rates and more excellent cycling stability cycled under high rates. The charge capacities of BDC-K electrode are 801, 710 and 643 mAh g^{-1} at the current rates of 0.1 C, 0.5 C and 1 C, respectively. The reversible capacity is still as high as 595 mAh g^{-1} after 500 cycles cycled under 1 C rate, which represents only 92.5% capacity retention. To our knowledge, this excellent rate capability is much better than that of some biomass-derived anodes of lithium ion batteries [55-57].

4. Conclusions

New carbonaceous materials derived from bean dregs were prepared using a pyrolysis method. Graphitization treatment and chemical activation are effective methods to improve the structure for carbon materials. A sample thermally treated at 2800 ^{O}C shows more ordered

graphitic domains and superior reversibility, excellent cycling stability and rate capability. Besides, the samples treated with $ZnCl_2$ and KOH possess high surface area and more developed porosity to provide more pathways for easy accessibility of electrolytes and faster transportation of lithium ions to deliver high capacities and behaving well both in cycling stability and rate capability. The results indicate that biomass-derived carbon from bean dregs holds a great promise for developing anode materials for lithium-ion batteries.

Acknowledgements

This work is supported by the National Nature Science Foundation of China (51272074) and the Natural Science Foundation of Hunan Province（2016JJ5041）.

References

[1] C. Li, X. Yin, L. Chen, Q. Li, T. Wang, Porous carbon nanofibers derived from conducting polymer: synthesis and application in lithium-ion batteries with high-rate capability, J. Phys. Chem. C 113 (30) (2009) 13438-13442.

[2] Y. Wu, E. Rahm, R. Holze, Carbon anode materials for lithium ion batteries, J. Power Sources 114 (2) (2003) 228-236.

[3] S. Wang, S. Yata, J. Nagano, Y. Okano, H. Kinoshita, H. Kikuta, T. Yamabe, A new carbonaceous material with large capacity and high efficiency for rechargeable Li-ion batteries, J. Electrochem. Soc. 147 (7) (2000) 2498-2502.

[4] H. S. Oktavian, K. Yamadab, K. Waki, Nano-drilled multiwalled carbon nanotubes: characterizations and application for LIB anode materials. J. Mater. Chem. 22 (0) (2012) 25167-25173.

[5] M. V. Reddy, G. V. S. Rao, B. V. R. Chowdari, Metal oxides & oxysalts as anode materials for Li ion batteries, Chem. Rev. 113 (7) (2013) 5364-5457.

[6] P. Poizot, S. Laruelle, S. Grugeon, L. Dupont, J. M. Tarascon, Nano-sized transition metal oxides as negative electrode material for lithium-ion batteries, Nature 407 (0)

(2000) 496-499.

[7] Y. Yan, Y. X. Yin, S. Xin, Y. G. Guo, L. J. Wan, Ionothermal synthesis of sulfur-doped porous carbons hybridized with graphene as superior anode materials for lithium-ion batteries, Chem. Commun. 48 (0) (2012) 10663-10665.

[8] E. Yoo, J. Kim, E. Hosono, H. S. Zhou, T. Kudo, I. Honma, Large reversible Li storage of graphene nanosheet families for use in rechargeable lithium ion batteries, Nano Lett. 8 (8) (2008) 2277-2282.

[9] C. Y. Wang, D. Li, C. O. Too, G. G. Wallace, Electrochemical properties of grapheme paper electrodes used in lithium batteries, Chem. Mater. 21 (13) (2009) 2604-2606.

[10] J. B. Chang, X. K. Huang, G. H. Zhou, S. M. Cui, P. B. Hallac, J. W. Jiang, P. T. Hurley, J. H. Chen, Multilayered Si nanoparticle/reduced graphene oxide hybrid as a high-performance lithium-ion battery anode, Adv. Mater. 26 (5) (2013) 758-764.

[11] Z. Q. Zhu, S. W. Wang, J. Du, T. R. Zhang, F. Y. Cheng, J. Chen, Ultrasmall Sn nanoparticles embedded in nitrogen-doped porous carbon as high-performance anode for lithium-ion batteries, Nano Lett. 14 (0) (2014) 153-157.

[12] S. Grugeon, S. Laruelle, R. Herrera-Urbina, L. Dupont, P. Poizot, J. M. Tarascon, Particle size effects on the electrochemical performance of copper oxides toward lithium, J. Electrochem. Soc. 148 (4) (2001) A285-A292.

[13] L. Zhang, H. B. Wu, B. Liu, X. W. (David) Lou, Formation of porous SnO_2 microboxes via selective leaching for highly reversible lithium storage. Energy Environ. Sci. 7 (0) (2014) 1013-1017.

[14] Y. Q. Zou, Y. Wang, Microwave solvothermal synthesis of flower-like SnS_2 and SnO_2 nanostructures as high-rate anodes for lithium ion batteries, Chem. Eng. J. 229 (0) (2013) 183–189.

[15] L. Zhang, H. B. Wu, S. Madhavi, H. H. Hng, X. W. (David) Lou, Formation of Fe_2O_3 microboxes with hierarchical shell structures from metal-organic frameworks and their lithium storage properties, J. Am. Chem. Soc. 134 (0) (2012) 17388-17391.

[16] L. Zhou, H. Y. Xu, H. W. Zhang, J. Yang, S. B. Hartono, K. Qian, J. Zou, C. Z. Yu, Cheap and scalable synthesis of α-Fe_2O_3 multi-shelled hollow spheres as high-performance anode materials for lithium ion batteries, Chem. Commun. 49 (77) (2013) 8695-8697.

[17] J. Cabana, L. Monconduit, D. Larcher, M. R. Palacín, Beyond intercalation-based Li-ion batteries: the state of the art and challenges of electrode materials reacting through conversion reactions, Adv. Mater. 22 (35) (2010) E170-E192.

[18] P. Zuoa, G. Yin, Z. Yang, Z. Wang, X. Cheng, D. Jia, C. Du, Improvement of cycle performance for silicon/carbon composite used as anode for lithium ion batteries, Mater. Chem. Phys. 115 (2) (2009) 757-760.

[19] M. Wakihara, Recent developments in lithium ion batteries, Mater. Sci. Eng. R., 33 (4) (2001) 109-134.

[20] M. Noel, V. Suryanarayana, Role of carbon host lattices in Li-ion intercalation /de-intercalation process, J. Power Sources 111 (2) (2002) 193-209.

[21] S. W. Han, D. W. Jung, J. H. Jeong, E. S. Oh, Effect of pyrolysis temperature on carbon obtained from green tea biomass for superior lithium ion battery anodes, Chem. Eng. J. 254 (0) (2014) 597-604.

[22] L. P. Wang, J. Xue, B. Gao, P. Gao, C. X. Mou, J. Z. Li, Rice husk derived carbon-silica

composites as anodes for Lithium ion batteries, RSC Adv. 4 (110) (2014) 64744-64746.

[23] Y. P. Guo, J. R. Qi, Y. Q. Jiang, S. F. Yang, Z. C. Wang, H. D. Xu, Performance of electrical double layer capacitors with porous carbons derived from rice husk, Mater. Chem. Phys. 80 (3) (2003) 704-709.

[24] T. K. F. George, C. L. Chen, High-capacity carbons for lithium-ion batteries prepared from rice husk, J. Power Sources 97 (0) (2001) 47-51.

[25] F. Zhang, K. X. Wang, G. D. Li, J. S. Chen, Hierarchical porous carbon derived from rice straw for lithium ion batteries with high-rate performance, Electrochem. Commun. 11 (1) (2009) 130-133

[26] T. E. Rufford, D. Hulicova-Jurcakova, K. Khosla, Z. H. Zhu, G. Q. Lu, Microstructure and electrochemical double-layer capacitance of carbon electrodes prepared by zinc chloride activation of sugar cane bagasse, J. Power Sources 195 (3) (2010) 912-918.

[27] T. E. Rufford, D. Hulicova-Jurcakova, Z. H. Zhu, G. Q. Lu, Nanoporous carbon electrode from waste coffee beans for high performance supercapacitors. Electrochem. Commun. 10 (10) (2008) 1594-1597.

[28] Y. J. Hwang, S. K. Jeong, J. S. Shin, K. S. Nahm, A. M. Stephan, High capacity disordered carbons obtained from coconut shells as anode materials for lithium batteries, J. Alloy. Compd. 448 (1) (2008) 141-147.

[29] G. T. K. Fey, D. C. Lee, Y. Y. Lin, T. P. Kumar, High-capacity disordered carbons derived from peanut shells as lithium-intercalating anode materials, Synthetic Met. 139 (1) (2003) 71-80.

[30] W. Xing, C. Liu, Z. Y. Zhou, L. Zhang, J. Zhou, S. P. Zhuo, Z. F. Yan, H. Gao, G. Q. Wang, S. Z. Qian, Superior CO2 uptake of N-doped activated carbon through hydrogen-bonding interaction, Energy Environ. Sci. 5 (6) (2012) 7323-7327.

[31] C. P. Ruan, K. L. Ai, L. H. Lu, Biomass-derived carbon materials for highperformance supercapacitor electrodes, RSC Adv. 4 (58) (2014) 30887-30895.

[32] F. Chen, J. Yang, T. Bai, B. Long, X. Y. Zhou, Biomass waste-derived honeycomb-like nitrogen and oxygen dual-doped porous carbon for high performance lithium-sulfur batteries, Electrochim. Acta 192 (0) (2016) 99-109.

[33] J. C. Arrebola, A. Caballero, L. Hernán, J. Morales, M. O. Marín, V. G. Serrano, Improving the performance of biomass-derived carbons in Li-ion batteries by controlling the Lithium insertion process, J. Electrochem. Soc. 157 (7) (2010) A791-A797.

[34] Y. Liu, J. S. Xue, J. R. Dahn, Mechanism of lithium insertion in hard carbons prepared by pyrolysis of epoxy resins, Carbon 34 (2) (1996) 193-200.

[35] A. Sadezky, H. Muckenhuber, H. Grothe, R. Niessner, U. Poschl, Raman microspectroscopy of soot and related carbonaceous materials: spectral analysis and structural information, Carbon 43 (8) (2005) 1731-1742.

[36] W. Huang, Y. Wang, G. Luo, F. Wei, 99.9% purity multi-walled carbon nanotubes by vacuum high-temperature annealing, Carbon 41 (13) (2003) 2585-2590.

[37] A. C. Dillon, M. Yudasaka, M. S. Dresselhaus, Employing Raman spectroscopy to qualitatively evaluate the purity of carbon single-wall nanotube materials, J. Nanosci. Nanotechnol. 4 (7) (2004) 691-701.

[38] Z. B. Lei, Y. Xiao, L. Q. Dang, W. S. You, Fabrication of ultra-large mesoporous carbon with tunable pore size by monodisperse silica particles derived from seed growth process,

Micropor. Mesopor. Mat. 96 (1) (2006) 127-134.
[39] K. Nakagawa, S. R. Mukai, K. Tamura, H. Tamon, Mesoporous activated carbons from phenolic resins, Chem. Eng. Res. Des. 85 (9) (2007) 1331-1337.
[40] Y. G. Guo, J. S. Hu, L. J. Wan, Nanostructured materials for electrochemical energy conversion and storage devices, Adv. Mater. 20 (15) (2008) 2878-2887.
[41] T. Doi, Y. Iriyama, T. Abe, Z. Ogumi, Lithium-ion transfer at a solid polymer electrolyte/non-graphitizable carbon electrode interface, J. Power Sources 142 (1) (2005) 329-332.
[42] H. H. Ru, N. B. Bai, K. X. Xiang, W. Zhou, H. Chen, X. S. Zhao, Porous carbons derived from microalgae with enhanced electrochemical performance for lithium-ion batteries, Electrochim. Acta 194 (0) (2016) 10-16.
[43] D. Zhou, Z. J. Liu, X. K. Lv, G. S. Zhou, J. Yin, Electrochemical studies of LiB compound as anode material for lithium-ion battery, Electrochim. Acta 51 (26) (2006) 5731-5737.
[44] E. Peled, V. Eshkenazi, Y. Rosenberg, Study of lithium insertion in hard carbon made from cotton wool, J. Power Sources, 76 (2) (1998) 153-158.
[45] I. Mochida, C. H. Ku, Y. Korai, Anodic performance and insertion mechanism of hard carbons prepared from synthetic isotropic pitches, Carbon 39 (3) (2001) 399-410.
[46] F. Cao, I. V. Barsukov, H. J. Bang, P. Zaleski, J. Prakash, Evaluation of graphite materials as anodes for lithium-ion batteries, J. Electrochem. Soc. 147 (10) (2000) 3579-3583.
[47] X. L. Wu, L. L. Chen, S. Xin, Y. X. Yin, Y. G. Guo, Q. S. Kong, Y. Z. Xia, Preparation and Li storage properties of hierarchical porous carbon fibers derived from alginic acid, ChemSusChem 3 (6) (2010) 703-707.
[48] J. Ou, Y. Zhang, L. Chen, H. Y. Yuan, D. Xiao, Heteroatom doped porous carbon derived from hair as an anode with high performance for lithium ion batteries, RSC Adv. 4(109) (2014) 63784-63791.
[49] Y. H. Zhu, X. X. Xiang, E. H. Liu, Y. H. Wu, H. Xie, Z. L. Wu, Y. Y. Tian, An activated microporous carbon prepared from phenol-melamine-formaldehyde resin for lithium ion battery anode, Mater. Res. Bull. 47 (8) (2012) 2045-2050.
[50] A. M. Stephan, T. P. Kumar, R. Ramesh, S. Thomac, S. K. Jeong, K. S. Nahm, Pyrolitic carbon from biomass precursors as anode materials for lithium batteries, Mat. Sci. Eng. A 430 (1) (2006) 132-137.
[51] Y. J. Hwang, S. K. Jeong, K. S. Nahm, J. S. Shin, A. M. Stephan, Pyrolytic carbon derived from coffee shells as anode materials for lithium batteries, J. Phys. Chem. Solids 68 (2) (2007) 182-188.
[52] J. Ding, H. Wang, Z. Li, K. Cui, D. Karpuzov, X. H. Tan, A. Kohandehghan, D. Mitlin, Peanut shell hybrid sodium ion capacitor with extreme energy–power rivals lithium ion capacitors, Energ. Environ. Sci. 8 (3) (2015) 941-955.
[53] D. Y. Zhai, H. D. Du, B. H. Li, Y. Zhu, F. Y. Kang, Porous graphitic carbons prepared by combining chemical activation with catalytic graphitization, Carbon 49 (2) (2011) 725-729.
[54] P. Kalyani, A. Anitha, Biomass carbon & its prospects in electrochemical energy systems, Int. Hydrogen Energ. 38 (10) (2013) 4034-4045.
[55] A. Caballero, L. Hernán, J. Morales, Limitations of disordered carbons obtained from

biomass as anodes for real lithium-ion batteries, ChemSusChem 4 (5) (2011) 658-663.
[56] Y. Zhang, F. Zhang, G. D. Li, J. S. Chen, Microporous carbon derived from pinecone hull as anode material for lithium secondary batteries, Mater. Lett. 61 (30) (2007) 5209-5212.
[57] X. L. Sun, X. H. Wang, N. F. Feng, L. Qian, X. W. Li, D. Y. He, A new carbonaceous material derived from biomass source peels as an improved anode for lithium ion batteries, J. Anal. Appl. Pyrol. 100 (0) (2013) 181-185.

Figure and table captions

Fig. 1 (a) XRD patterns, (b) Fitted Raman spectra (c) N_2 adsorption isotherms and (d) Pore-size distribution curves of BDCs and SEM images of (e) BDC-700, (f) BDC-900, (g) BDC-1100.

Fig. 2 Galvanostatic discharge/charge curves of (a) BDC-700, (b) BDC-900 and (c) BDC-1100 electrodes cycled at a rate of 0.1 C; Cyclic voltammograms of (d) BDC-700, (e) BDC-900, and (f) BDC-1100 at a scan rate of 0.1 mV s^{-1} in the voltage range of 0.0-2.0 V; (g) Cycling performance of the BDC-900 electrode tested at a rate of 0.1C; (h) Rate performance of the BDC-900 electrode over cycling at rates of 0.1 C, 0.5 C and 1 C, respectively.

Fig. 3 (a) XRD pattern and (b) Fitted Raman spectra of BDC-2800; SEM images of (c) BDC-2800; and corresponding TEM and HRTEM images of (d-f) BDC-900 and (g-i) BDC-2800.

Fig. 4 (a) Galvanostatic discharge/charge curves of BDC-2800 electrode cycled at a rate of 0.1 C; (b) Cycling performance of BDC-2800 electrode at a rate of 0.1 C; (c) Rate capability of BDC-2800.

Fig. 5 (a) XRD patterns, (b) Raman spectra (c) N_2 adsorption isotherms and (d) Pore-size distribution curves obtained from BDC-Z and BDC-K; SEM images of (e) BDC-Z and (f) BDC-K.

Fig. 6 Charge/discharge curves of (a) BDC-Z and (b) BDC-K electrodes; (c) Cycling stability of BDC-Z and BDC-K electrodes tested at a rate of 0.1 C for 100 cycles; (d) Rate performance of BDC-Z and BDC-K electrodes compared with BDC-900 electrode

tested at rates of 0.1 C, 0.5 C and 1 C, respectively.

Table 1 Elemental composition information for BDC-700, BDC-900 and BDC-1100

Table 2 Structure and textural properties of BDC-700, BDC-900 and BDC-1100

Table 3 Structure and textural properties of BDC-900 and BDC-2800

Table 4 Structure and textural properties of BDC-900, BDC-Z and BDC-K

Figure 1

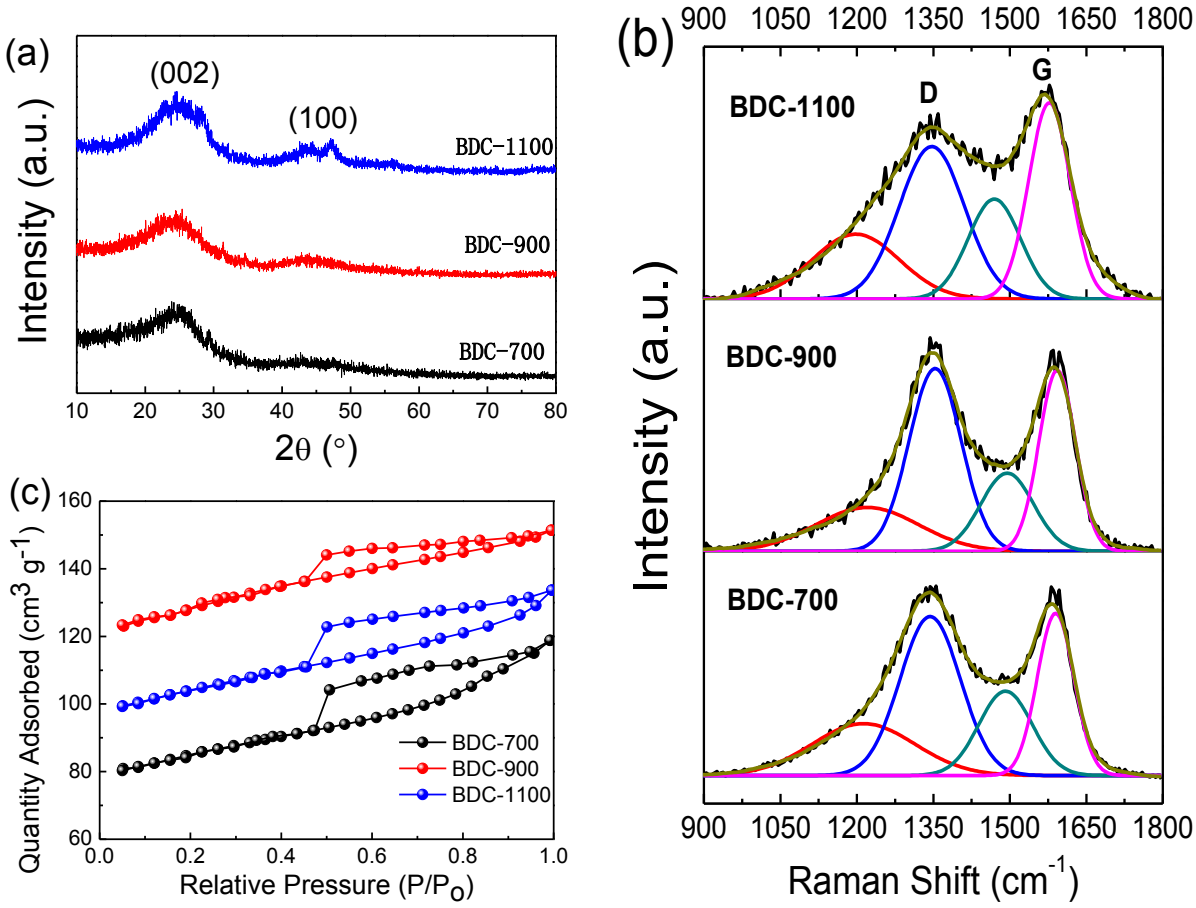

Figure 2

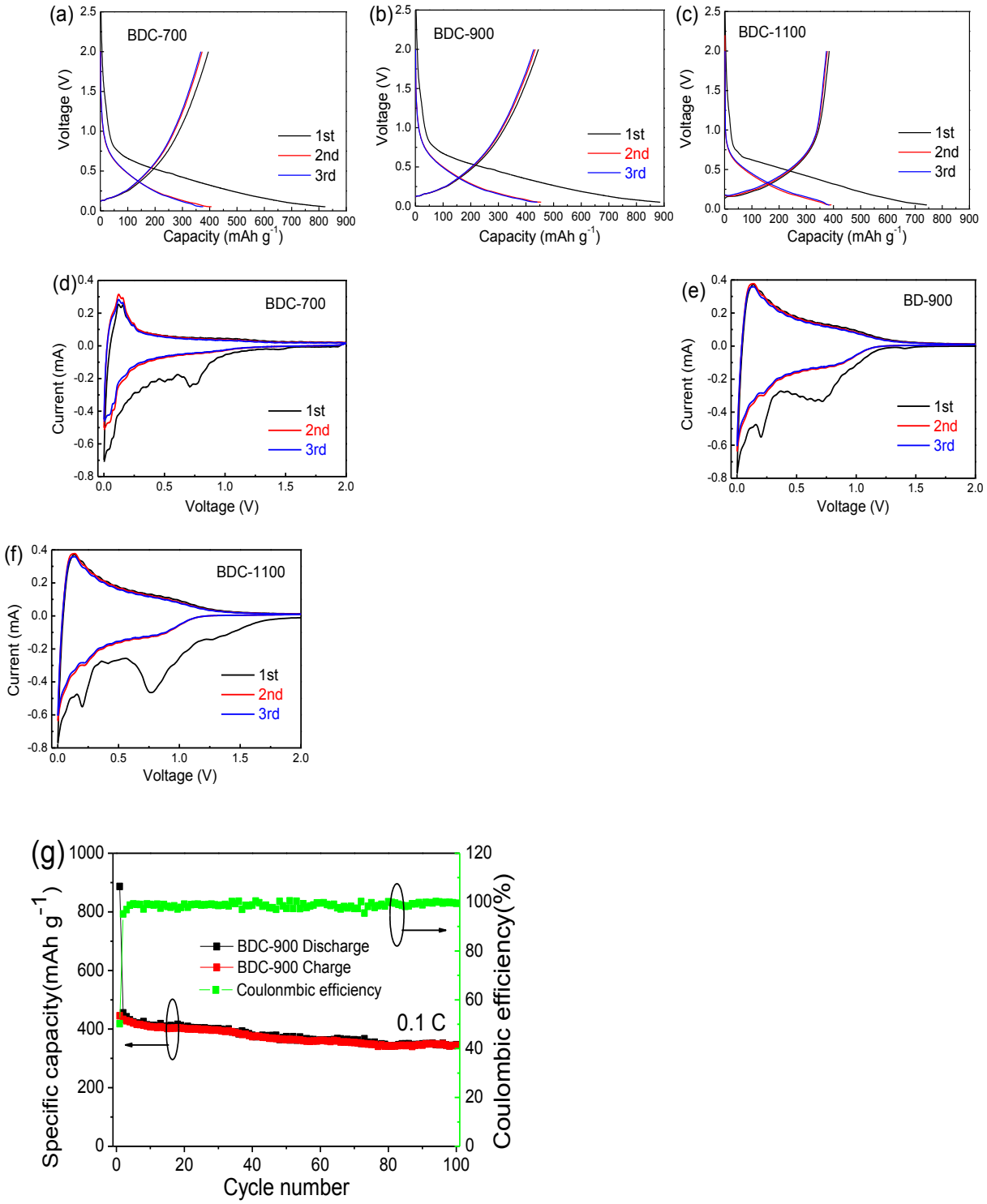

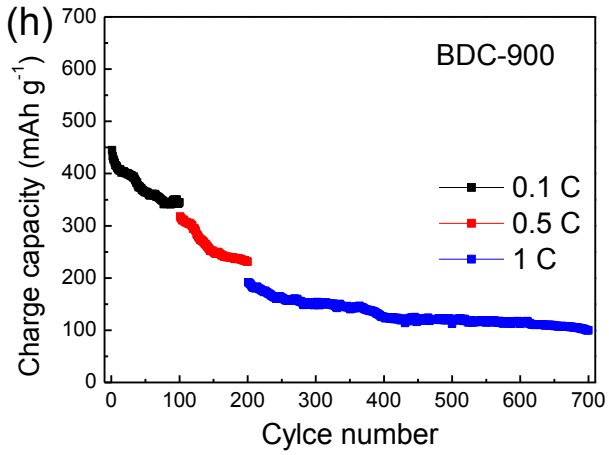

Figure 3

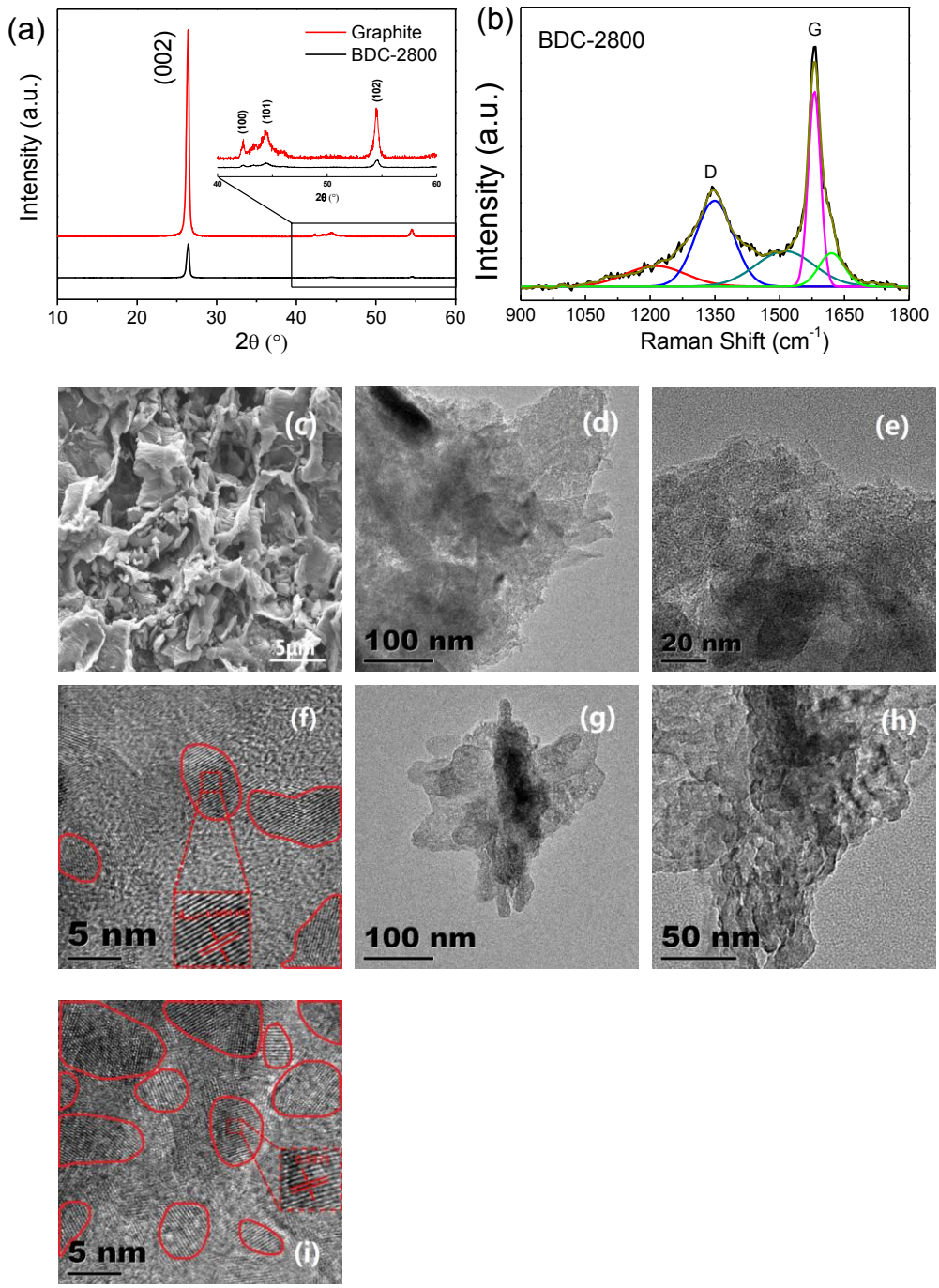

Figure 4

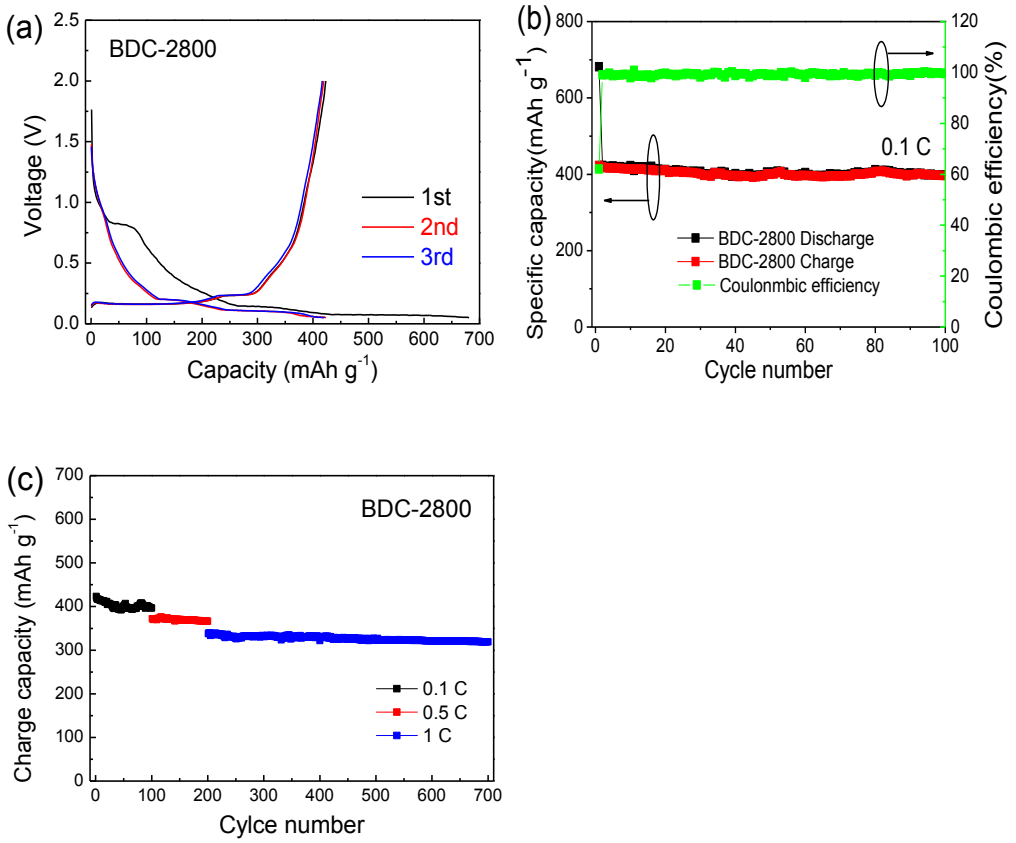

Figure 5

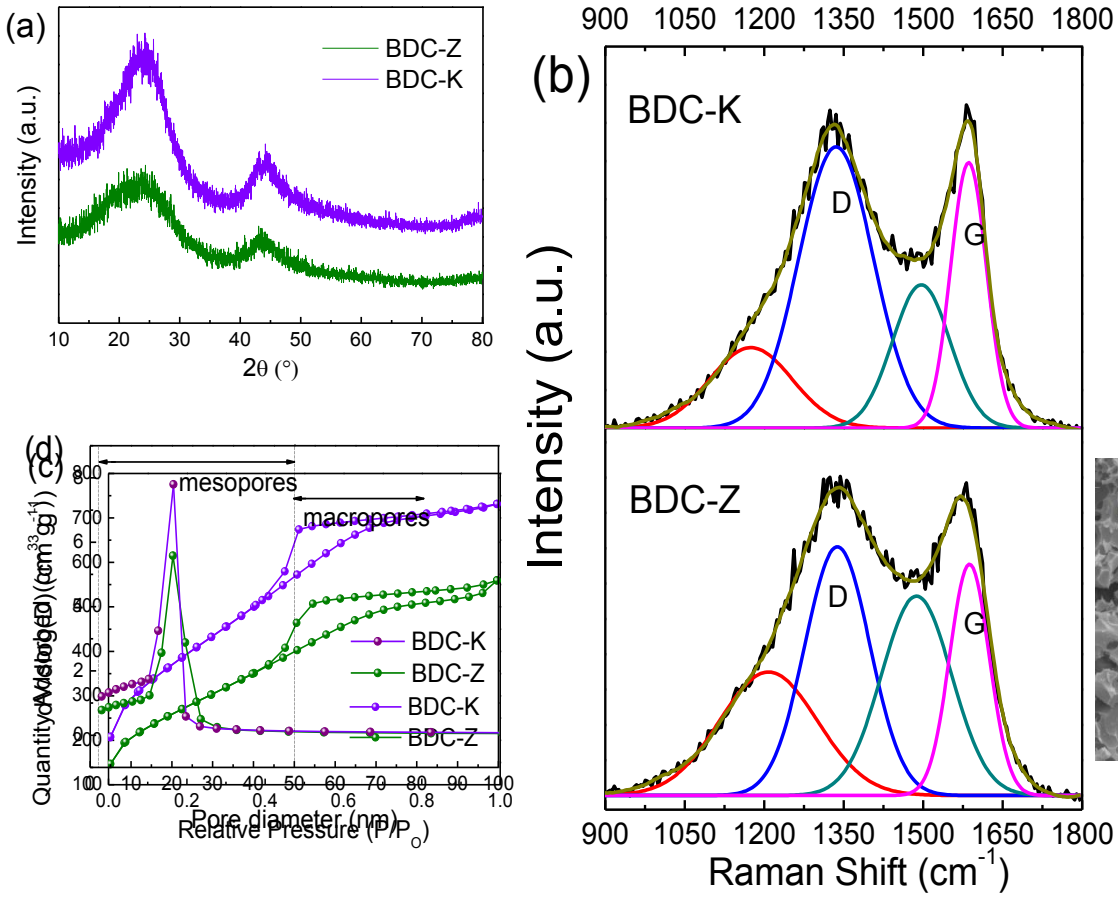

Figure 6

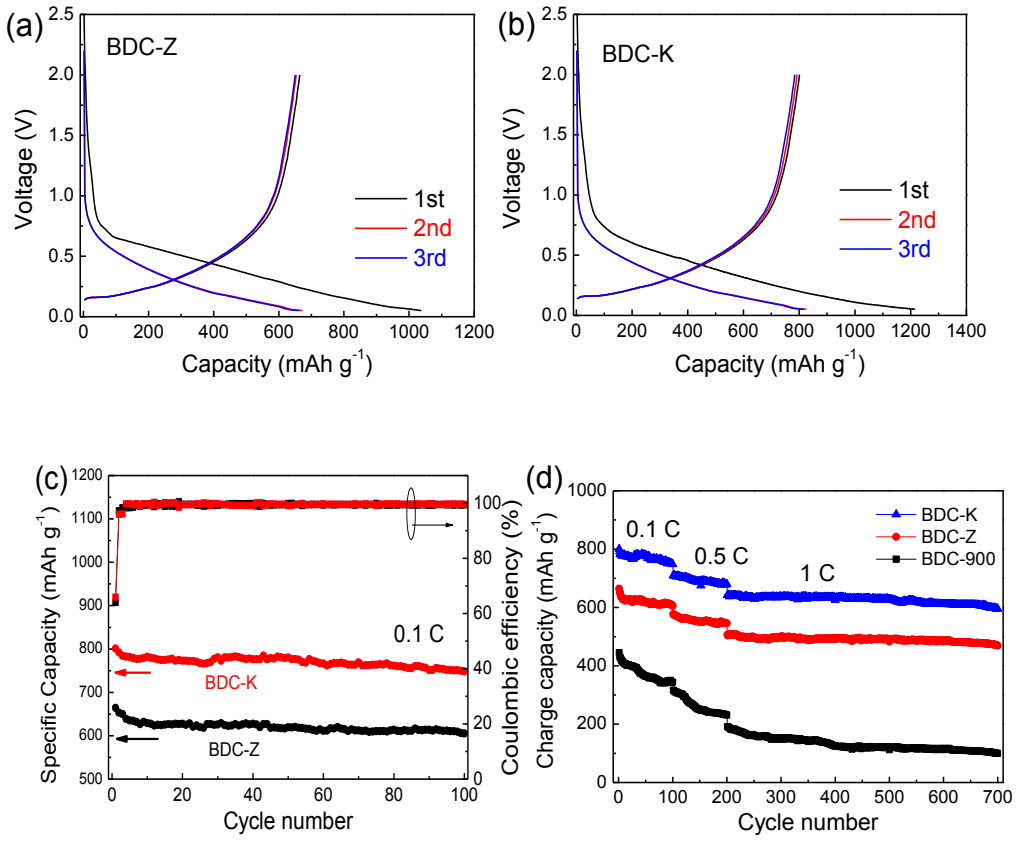

Table

Table 1 Elemental composition information for BDC-700, BDC-900 and BDC-1100

Sample	Elemental analysis				EDX microanalysis		
	C%	N%	O%	H%	C%	N%	O%
BDC-700	76.50	4.65	16.51	1.71	79.84	4.69	12.06
BDC-900	84.87	1.05	11.68	1.39	86.54	3.59	8.26
BDC-1100	87.32	0.80	10.09	1.00	87.49	2.28	9.03

Table 2 Structure and textural properties of BDC-700, BDC-900 and BDC-1100

Sample	d_{002}	La	Lc	I_G/I_D	S_{BET}	Pore volume	Average pore diameter
	(nm)	(nm)	(nm)		(m^2/g)	(cm^3/g)	(nm)
BDC-700	0.3851	2.55	0.76	0.79	180	0.1152	19.34
BDC-900	0.3694	3.17	0.85	0.82	269	0.1676	15.69
BDC-1100	0.3573	3.53	1.16	1.10	113	0.0984	21.59

Table 3 Structure and textural properties of BDC-900 and BDC-2800

Sample	d_{002}	L_a	L_c	I_G/I_D
	(nm)	(nm)	(nm)	
BDC-900	0.3694	3.17	0.85	0.82
BDC-2800	0.3371	34.16	21.64	2.30

Table 4 Structure and textural properties of BDC-900, BDC-Z and BDC-K

Sample	d_{002}	L_a	L_c	I_G/I_D	S_{BET}	Pore volume	Average pore diameter
	(nm)	(nm)	(nm)		(m^2/g)	(cm^3/g)	(nm)
BDC-900	0.3694	3.17	0.85	0.82	269	0.1676	15.69
BDC-Z	0.3830	3.40	0.88	0.56	827	1.0397	37.53
BDC-K	0.3748	4.12	0.87	0.45	1139	1.1436	26.34